Hydrogen wettability and capillary pressure in Clashach sandstone for underground hydrogen storage

Eike M. Thaysen[1,2], Zaid Jangda[3], Aliakbar Hassanpouryouzband[1], Hannah Menke[3], Kamaljit Singh[3], Ian B. Butler[1], Niklas Heinemann[1], Katriona Edlmann[1]

[1]School of Geoscience, Grant Institute, The King's Buildings, The University of Edinburgh, James Hutton Road, Edinburgh, EH9 3FE, United Kingdom

[2]Department of Geosciences, Institute of Environmental Assessment and Water Research (IDAEA), Severo Ochoa Excellence Center of the Spanish Council for Scientific Research (CSIC), Jordi Girona 18–26, 08034 Barcelona, Spain

[3]Institute of GeoEnergy Engineering, Heriot-Watt University, EH14 4AS, Edinburgh, UK

Hydrogen wettability and capillary pressure in Clashach sandstone for underground hydrogen storage

Eike M. Thaysen[1,2], Zaid Jangda[3], Aliakbar Hassanpouryouzband[1], Hannah Menke[3], Kamaljit Singh[3], Ian B. Butler[1], Niklas Heinemann[1], Katriona Edlmann[1]

[1]School of Geoscience, Grant Institute, The King's Buildings, The University of Edinburgh, James Hutton Road, Edinburgh, EH9 3FE, United Kingdom

[2]Department of Geosciences, Institute of Environmental Assessment and Water Research (IDAEA), Severo Ochoa Excellence Center of the Spanish Council for Scientific Research (CSIC), Jordi Girona 18–26, 08034 Barcelona, Spain

[3]Institute of GeoEnergy Engineering, Heriot-Watt University, EH14 4AS, Edinburgh, UK

ABSTRACT

Hydrogen (H_2) can support the transition to net-zero carbon (C) emissions by facilitating increased renewable energy use by acting as an energy store to balance supply and demand. Underground H_2 storage in porous media is investigated due to its high capacity and economical price. An important unknown in underground porous media H_2 storage is the volume of recoverable H_2 which is partly controlled by the H_2 wettability. Current H_2 contact angle data in sandstone systems span large ranges and fall short of clarifying if H_2 wettability changes with pressure.

We computed novel in-situ receding and advancing contact angles for the H_2-brine-Clashach sandstone system at pore fluid pressures of 2-7 MPa and for nitrogen (N_2)-brine-Clashach sandstone at 5 MPa, based on X-ray microtomography images of gas displacement and trapping in Clashach sandstone. A centrifuge analysis of the capillary pressure (P_c) at varying water saturations was conducted for N_2. The H_2 P_c curve was derived from the N_2 P_c, the N_2 wettability measurements, and existing information on the density differential between brine and H_2 and N_2 and the interfacial tensions of these gases.

The results show no change of the H_2-brine-Clashach sandstone contact angles within the examined pressure range, with mean receding (drainage) and advancing (imbibition) contact angles of 61°± 24-26° and 58°± 20-22°, respectively, at all pore fluid pressures, indicating a water-wet rock and implying that based on the wettability alone, no decrease in H_2 recovery with increasing pressure (i.e. reservoir depth) is expected. While residual trapping was consistent with trapping in water-wet systems, the observed increase in residual trapping at 7 MPa requires further investigation. Alignment with other wettability studies in sandstone systems indicates that for contact angles around 60-70°, wettability may not always be the main

control for the H_2 saturation in the pore space but that H_2 dissolution and channeling events may significantly affect those parameters. Further, contact angle measurements in artificial systems significantly underestimate in-situ contact angles as provided by this study, highlighting the need for microtomography-based wettability investigations. We found relatively low irreducible water saturations of 12.6-14.0% at H_2 P_c of 0.43 MPa, suggesting a favorable H_2 relative permeability in Clashach and high H_2 storage capacity. Our results provide detailed insights into the controls on H_2 displacement and capillary trapping as well as crucial input parameters for the modelling and design of H_2 storage operations in porous media.

KEYWORDS Hydrogen, underground storage, µCT, wetting state, capillary pressure, flow experiments, nitrogen

GRAPHICAL ABSTRACT

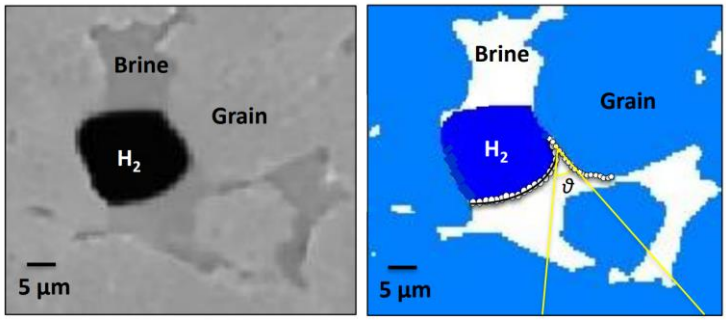

1. INTRODUCTION

Climate change is a major problem of increasing global relevance that will have wide ranging adverse implications for all life on Earth [1, 2]. In order to mitigate climate change we must reduce our reliance on fossil fuels, which currently account for over 75% of our greenhouse gas emissions, reduce atmospheric carbon dioxide (CO_2) concentrations and transition to a low carbon (C) society [1]. This requires the implementation of passive and active CO_2 sequestration technologies (e.g., [3-5]), and an increase in the proportion of renewable energy such as wind and solar energy into the near future. A major challenge for renewable energy is the imbalance between supply and demand [6]. A way of overcoming this imbalance is the generation of H_2 via electrolysis of water during periods of renewable energy oversupply with subsequent underground H_2 storage [7, 8] that allows for recovery and use of H_2 as an energy source during periods of renewable energy shortage. Electricity generation from stored H_2 could balance seasonal electricity demands, yet the low energy density of H_2 requires large-scale storage capacities that are only available in geological media [9]. While underground storage of H_2 in salt caverns plays an important part in the daily and weekly reduction of energy imbalances, seasonal balancing may only be achieved with H_2 storage in underground porous media including depleted gas fields and saline aquifers that have TWh storage capacities [9, 10].

Emerging evidence suggests there are no important showstoppers for the implementation of porous media H_2 storage [11-19]. Yet, certain knowledge gaps remain to be addressed, amongst them the H_2 fluid flow behavior in the porous medium, which, along with the injected cushion gas, governs gas injectivity and recovery from the reservoir [9, 20] and hence the economic viability of the storage operation. Of particular importance for describing the H_2 fluid flow in the porous medium is determinations of capillary pressure, *Pc*, and relative permeability, *kr*, [21] as well as quantification of H_2 saturation and trapping inside rocks, which can be achieved

through pore-scale visualization studies [22]. These factors directly relate to the fluids present inside the porous medium and inform simulation models to predict H_2 displacement and trapping and upscaling to the reservoir scale.

The key parameter for controlling multiphase fluid flow in porous media is wettability [23]. Wettability is characterized as the spatial distribution of the contact angle, θ, at the contact line between two fluids and the solid matrix. It is measured through the densest fluid, with a contact angle of 0 reflecting a perfectly wetting fluid [24, 25]. Wettability influences flow dynamics such as P_c and irreducible water saturation, S_{wi}, and kr (Eq. 1), all of which in turn are influenced by the pore network morphology, connectivity and tortuosity.

$$P_c = \frac{2\gamma cos\theta}{r_c} = p_t - p_{cs} \ln\left(\frac{S_w - S_{wi}}{1 - S_{wi}}\right) = \frac{dv_{inj} * L * (\mu_g / K)}{k_r} \quad (1)$$

where γ denotes the interfacial tension (IFT) between the non-wetting phase and the wetting phase, r_c is the radius of the interface, p_t is the threshold pressure (i.e. the pressure at which the non-wetting phase is allowed to flow), p_{cs} is a parameter that controls the shape of the capillary pressure function, S_w is the saturation of the wetting phase (water), v_{inj} is the Darcy velocity, L is the length of the core, μ_g is the gas viscosity and K is the absolute permeability. Accurate knowledge of wettability over geological conditions (e.g. rock mineralogy, brine composition, pressure, temperature) is key for the design and optimization of H_2 storage projects [26].

Investigations of H_2 contact angles in sandstone systems or pure quartz span a large range of 0° to 75° [16, 27-35], which may be ascribed to differences in the measurement methodology, the experimental conditions, sample preparation and whether hysteresis was studied. In addition, there is a discrepancy in the effect of pressure on H_2 contact angles. While Hashemi et al. [28], and Higgs et al. [27] reported contact angles of 25-45° in Bentheimer and Berea sandstones without meaningful pressure or temperature correlations of the contact angle (captive-bubble method, 0.7-10 MPa and 20-60 °C), Iglauer et al. [29] reported an increase of

H_2/brine/quartz contact angles of 10-15° with a pressure increase from 10 to 15 MPa using the tilted plate method.

Similar discrepancies are also found in H_2 relative permeabilities studies. Rezaei et al. [17] showed that shallower i.e. lower pressure sites are recommended for future H_2 storage operations in porous media due to a reduced relative permeability at higher H_2 saturations and high pressures of 10.7-20.7 MPa (unsteady state method, vertical core). This contrasts with previous findings by Yekta et al. [32] who documented little change of the H_2 relative permeability at pressure increases from 5.5 MPa to 10 MPa using the steady state technique. In addition, Rezaei et al. [17] showed good similarity between H_2 and N_2 relative permeability curves, while Lysyy et al. [36], Al-Yaseri et al. [37] and Zhang et al. [31] report divergent displacement behavior of H_2 and N_2. Thaysen et al. [11] reported similar displacement behavior of H_2 and N_2 during drainage but the residual saturation after imbibition, S_{nwr}, was much higher for N_2.

In this work, we assessed the discrepancy in the literature with regards to the effect of pressure on the H_2 wettability in sandstone, and relate acquired contact angle data to H_2 saturations in the pore space, to identify a possible control of wettability on the H_2 injectivity and recovery. We used previously acquired X-ray microtomography (µCT) images of H_2 and brine core-flood experiments in a Clashach sandstone at 2-7 MPa pore fluid pressure and ambient temperature (293 K) [11] to determine *in-situ* macroscopic H_2/brine/Clashach sandstone contact angles after drainage, $\theta_{receding}$, and imbibition, $\theta_{advancing}$. We hypothesized that $\theta_{advancing}$ would decrease with increasing pore fluid pressure, corresponding to previous observations of increased trapping at higher pressure [11]. Using µCT-images of N_2 and brine core-flood experiments in a Clashach sandstone at 5 MPa, we further quantified N_2/brine/Clashach sandstone contact angles. Measurements of the P_c at varying brine saturation for N_2 were conducted and results were combined with the N_2 wettability during drainage, as

well as with existing information on the density differential and the interfacial tensions between brine and H_2 and N_2, to calculate the H_2 P_c.

The current study stands out from other investigations due to three distinctive features. First, it represents the first experimental investigation of the H_2 wettability and P_c curve in Clashach sandstone. Second, no study has hitherto explored *in-situ* H_2 contact angles as a function of different pore fluid pressures and related this to the H_2 saturation in the pore space, effectively enabling the identification of a control of the wettability on the H_2 injectivity and recovery. Third, the visualization of the H_2 in the pore space via μCT allows for the investigation of controls on the S_{nwr} other than wettability, such as initial saturation, S_{nwi}, initial connectivity and channeling. As such, this study was tailored to provide detailed insights into the controls on H_2 displacement and capillary trapping. We show that, for the same rock sample, the $\theta_{advancing}$ did not change with pore fluid pressure, indicating that, based on the wettability alone, no change in H_2 trapping with increasing pressure is expected. Observed higher S_{nwr} at increased pressure were likely instigated by a decreased connectivity after drainage. This work pioneers a high-precision H_2 capillary pressure curve for Clashach sandstone with H_2 P_c of 0.43 MPa at S_{wi} of 12.6-14.0%, which suggests a favorable H_2 relative permeability in Clashach and high H_2 storage capacity. Our results may serve to inform the basic models for appropriate understanding of gas storage operations, as well as to influence their designs and predictions.

2. MATERIALS AND METHODS

2.1 Core Flood Experiments

Two-phase non-steady core flooding experiments at 2-7 MPa pore fluid pressure and ambient temperature (~293 K) by Thaysen et al. [11] were used as input data for this wettability study. In short, the H_2 (purity 99.9995 vol.%, BOC Ltd.) and brine (0.5 M CsCl, Sigma-Aldrich)

injections used the same untreated Clashach sandstone outcrop sample of 4.7 mm diameter and a length of 57 mm. The composition of Clashach is ~96 wt.% quartz, 2% K-feldspar, 1% calcite, 1% ankerite [38], porosity 11.1-14.4% [38-40]. For all experiments, the same water-wet Clashach sandstone plug was first saturated with brine at a flow rate of 70 µl min^{-1}. Afterwards, H_2 was injected (drainage) into the brine-saturated Clashach sandstone plug at a flow rate of 20 µl min^{-1}, based on desired capillary-regime capillary numbers, N_C, of 1.7×10^{-8} (see Thaysen et al. [11]). Subsequently, brine was reinjected (imbibition) at a flow rate of 20 µl min^{-1}, resulting in N_C of 2.4×10^{-6} [11]. One experiment at 5 MPa and 298 K used N_2 instead of H_2. The N_C of the N_2 experiment was 3.5×10^{-8} [11]. At the end of each experiment (one drainage and imbibition cycle), the Clashach sandstone sample was depressurized, following reinjection of brine to ensure that all H_2 was removed from the core to prepare for subsequent experiments. 3D volumes were acquired with µCT from the lower central portion of the sample at the end of each injection step (ten pore volumes). Images were processed as described in Thaysen et al. [11].

2.2 Wettability Analysis

The wettability was characterized for one of each duplicate H_2 experiment carried out at 2, 5 and 7 MPa (see asterisks in Fig. 1) and for the N_2 experiment (Fig. 1g) by measuring the gas/brine/Clashach sandstone contact angles through the brine phase on each voxel at the three-phase contact line on a sub-volume of 500 μm^3 using a highly accurate, widely-applied algorithm for automatic contact angle measurement of µCT-images [41]. The algorithm identifies and meshes the interfaces throughout the segmented stack of images and then reduces noise and imposes a constant curvature by smoothing the data. Subsequently, two normal vectors are placed at each contact point and the dot product of these vectors (where they meet

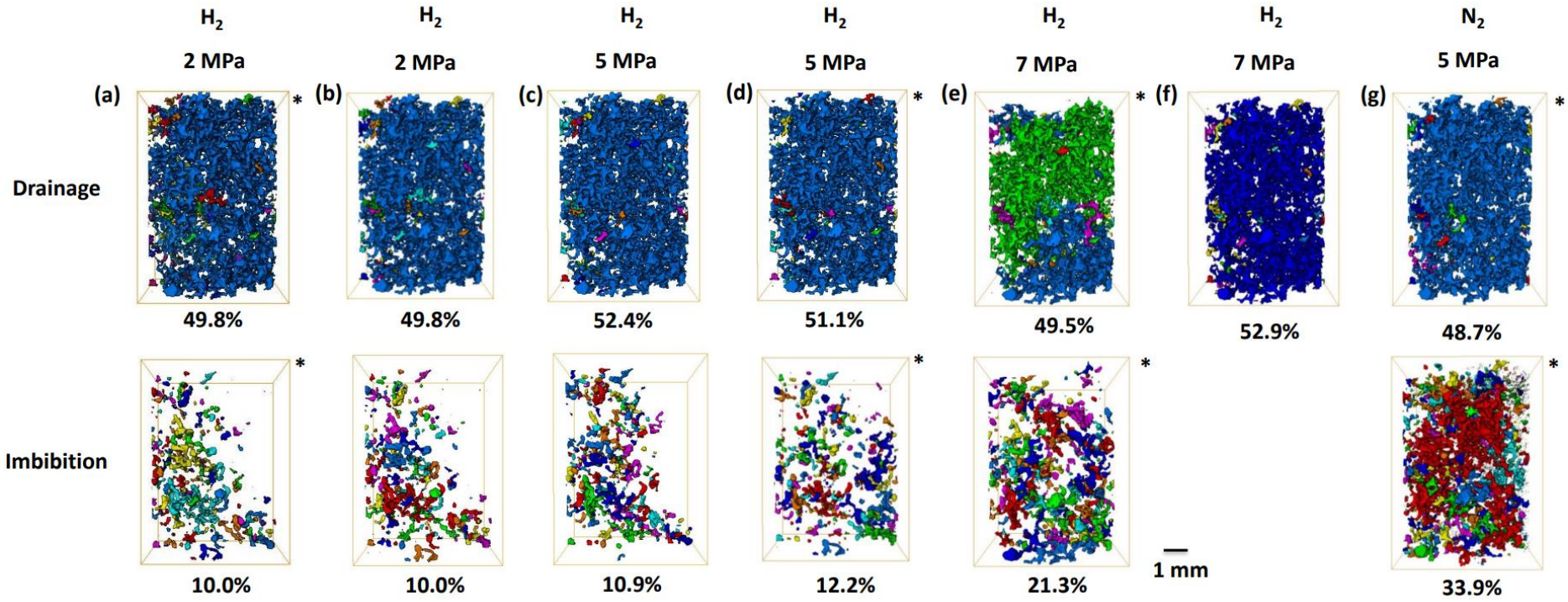

196

197 Figure 1. 3D renderings of gas clusters with gas saturation percentages in the pore space after drainage and primary imbibition at 2-7 MPa. Discrete
198 clusters were rendered in colors, where mainly one color marks one large, connected cluster and different colors indicate several, not connected
199 clusters. (a-b) H_2 at 2 MPa, (c-d) H_2 at 5 MPa and (e-f) H_2 at 7 MPa, (g) N_2 at 5 MPa, all at a constant flow rate of 20 µl min^{-1}. Asterisks mark
200 data utilized for the contact angle analysis. The imbibition experiment in (f) could not be visualized due to a filament burnout on the CT scanner.
201 Adapted from Thaysen et al. [11].

at the contact line) is used to determine the contact angle at each contact point along the contact line [41]. Data dispersion in contact angle measurements was calculated as the standard deviations of the mean. Example raw image slices of the subvolume and respective segmentations are shown in SI Fig. S1.

2.3 Hydrogen Capillary Pressure (P_{cH2})

The obtained N_2 wettability data (section 2.2) were combined with capillary pressure measurements with N_2 displacing brine, and converted into H_2 capillary pressure in order to further characterize the H_2 storage capacity in Clashach sandstone. In practice, the N_2 capillary pressure was determined using the high-speed centrifuge method [42] on two Clashach core plugs that were drilled from the same outcrop rock as the one sample used for the core flood experiments (see Supporting Information (SI) for method details). A comprehensive description of the P_c measurement for air is provided in the SI Text S1. To compute the P_{cH2} from the air P_c, we employed the recently published conversion factor, $\psi N_2/H_2$ [43]. The conversion factor reflects the variations in buoyancy forces, interfacial tensions, and contact angles between the two systems under study. This methodology offers enhanced utility compared to first-principle estimations, primarily because it eliminates the need to approximate pore throat radii, a process that typically introduces uncertainties of significant magnitude. The conversion factor is given by [43]:

$$\Psi_{\mathrm{N_2/H_2}} = \frac{\Delta\rho_{\mathrm{N_2/water}}}{\Delta\rho_{\mathrm{H_2/water}}} \frac{\gamma_{\mathrm{H_2/water}}}{\gamma_{\mathrm{N_2/water}}} \frac{\cos\theta_{H_2/\mathrm{water}}}{\cos\theta_{\mathrm{N_2/water}}} \quad (1)$$

where $\Delta\rho_{N2/water}$ and $\Delta\rho_{H2/water}$, represent the density differential between the gases and saline water under reservoir conditions. Brine density was deduced using the Danesh method [44]. The terms $\gamma_{N2/water}$ and $\gamma_{H2/water}$, denote the interfacial tension (IFT) between the gases and water and made use of the methodology for calculation of the IFT by Meybodi et al. [45], as previously detailed [43]. The last terms, $cos\theta_{N2/water}$ and $cos\theta_{H2/water}$, represent the wettability of

227 the Clashach sandstone samples. With this conversion factor in place, the P_{cH2} at varying water
228 saturations is ascertained by Eq. 2

229 $$Pc_{\mathrm{H_2}} = \Psi_{\mathrm{N_2/H_2}} \times Pc_{\mathrm{N_2}} \quad (2)$$

230 All parameters used to calculate the $\psi N_2/H_2$ and P_{cH2} are provided in SI Table S2.

231

232

233 3 RESULTS

234 *3.1 H_2-brine-Clashach sandstone contact angles relative to H_2 pore space saturations*

235 Hydrogen-brine-Clashach sandstone contact angles were normally distributed and showed
236 $\theta_{receding}$ of 61° at all three investigated pore fluid pressures, with standard deviations of 24°, 26°
237 and 24° at 2, 5 and 7 MPa pore fluid pressure, respectively (Fig. 2a). $\theta_{advancing}$ were 58 ± 21°,
238 58± 22° and 58 ± 20° at 2, 5 and 7 MPa pore fluid pressure, respectively (Fig. 2b). Initial H_2
239 saturation was ~ 50% at all pore fluid pressures (Fig. 1). Trapped H_2 in the pore space after
240 imbibition increased from 10-12% at 2-5 MPa to 21% at 7 MPa (Fig. 1), with a significant
241 cluster build-up at 7 MPa (Fig. 1e). The total mass of trapped H_2 at 2, 5 and 7 MPa, considering
242 saturation and density differences with pressure, was 0.022 mg, 56.3-67.6 mg and 165.6 mg,
243 respectively, in a pore volume of 138.5 mm^3.

244

245 *3.2 N_2-brine-Clashach sandstone contact angles relative to N_2 pore space saturations*

246 Nitrogen-brine-Clashach sandstone contact angles were normally distributed and were 66° ±
247 21° and 62° ± 24° after drainage and imbibition, respectively, at 5 MPa pore fluid pressure
248 (Fig. 3). Initial and residual saturations of N_2 were 49% and 34%, respectively (Fig. 1g).

249

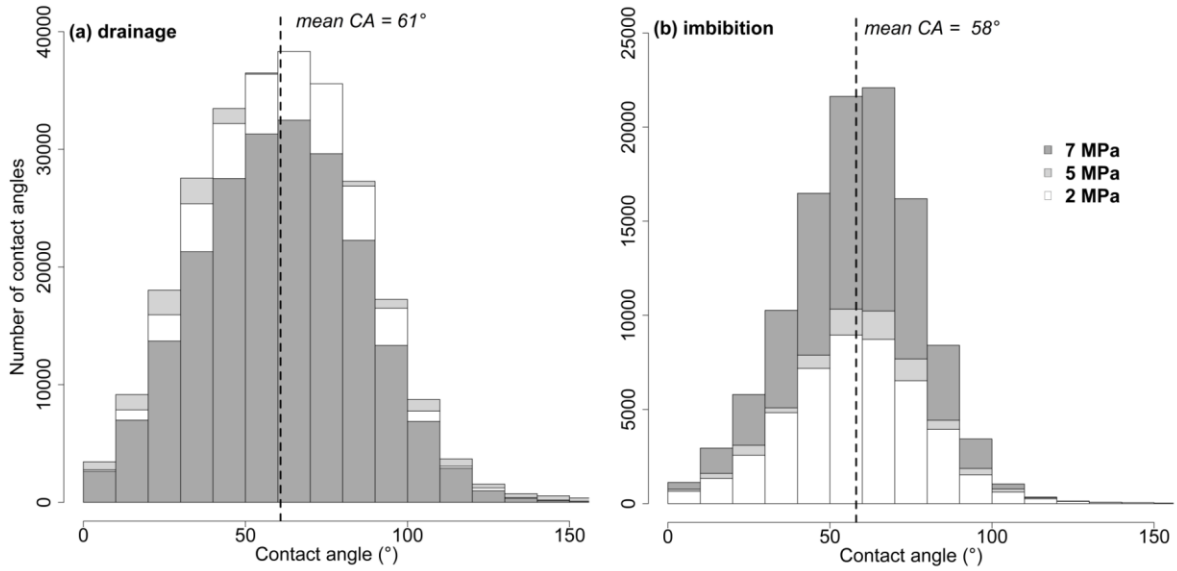

Figure 2. Drainage (a) and imbibition (b) contact angle distributions measured at the H_2/brine/Clashach sandstone interface at 2, 5 and 7 MPa pore fluid pressure. Note the different y-axes scales. The number of contact angles in these graphs is proportional to the H_2 saturation in the pore space. During drainage, a mean contact angle of 61° was observed at all pressures and H_2 saturation in the pore space was similar. During imbibition, the mean contact angle was 58° at all pore fluid pressures and a larger volume of H_2 was trapped at 7 MPa relative to at lower pressures.

3.3 P_c and irreducible water saturation

Figure 4 shows the drainage P_c curve for H_2 for two Clashach sandstone plugs with permeabilities of 139 mD and 178 mD, respectively. Under ambient conditions, P_{cH2} is approximately 1.3 to 1.36 times greater than that of N_2 (SI Table S2). The most pronounced impact on P_c stems from differences in wettability, contributing to approximately 19% of the effect (SI Table S2). The IFT and density differential between H_2 and N_2 relative to brine contribute less to the differences in P_c, as IFT for both H_2 and N_2 exhibit a variation of less than 8% and the density differential is less than 3% (SI Table S2). The irreducible water saturation

of Clashach sandstone is 12.6-14% and is reached at 0.43 MPa and 0.35 MPa for H_2 and N_2, respectively (Fig. 4, SI Table S2).

4. DISCUSSION

4.1 H_2-brine-Clashach sandstone contact angles

We observed normal distributions of $\theta_{receding}$ and $\theta_{advancing}$ (Fig. 2). If the solid surface was truly smooth and mineralogically homogeneous, all contact angles would be identical. The pore walls of naturally occurring rocks however are characterized by a certain surface roughness and mineralogical heterogeneity; hence, contact angles in real rock samples show some scatter, creating a distribution of contact angles [24]. In addition, the image resolution of 5.4 um^3 of the µCT images implies an inability to completely resolve the three-phase contact line which could cause segmentation errors and contact angle measurement errors, contributing to the observed large range of contact angles. Resolution limitations on contact angle measurements manifest

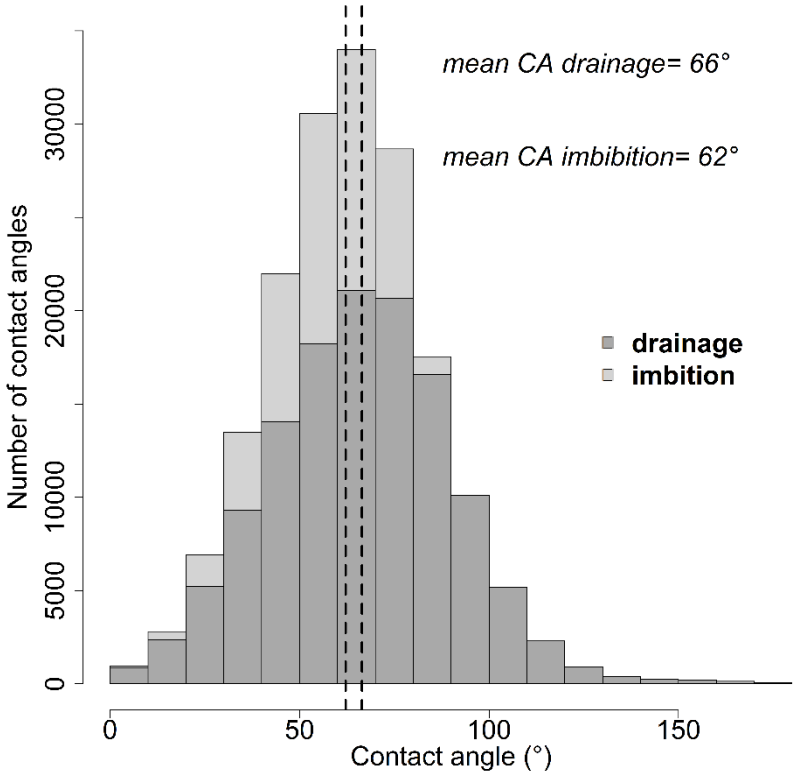

Figure 3. Contact angle distributions at the N_2/brine/Clashach sandstone interface after drainage and imbibition at 5 MPa pore fluid pressure showing average contact angles of 66° and 62°, respectively.

in particular during drainage when the saturation of the nonwetting phase increases and the fluid-fluid interfaces move into the pore throats where the voxel count is limited [46].

Considering standard deviations of 20-26° in the H_2 contact angle measurements, the mean drainage and imbibition contact angles of 61° and 58°, respectively (Fig. 2), were not significantly different. Standard deviations are within the upper range of the standard deviations reported in the literature for the here applied 3D local method [16, 27]. Contact angles are generally expected to be larger for imbibition than for drainage [21]. The here observed a higher drainage contact angle is probably an artefact caused by resolution limitation to our measurements, as observed for other in-situ H_2 contact angle measurements [31].

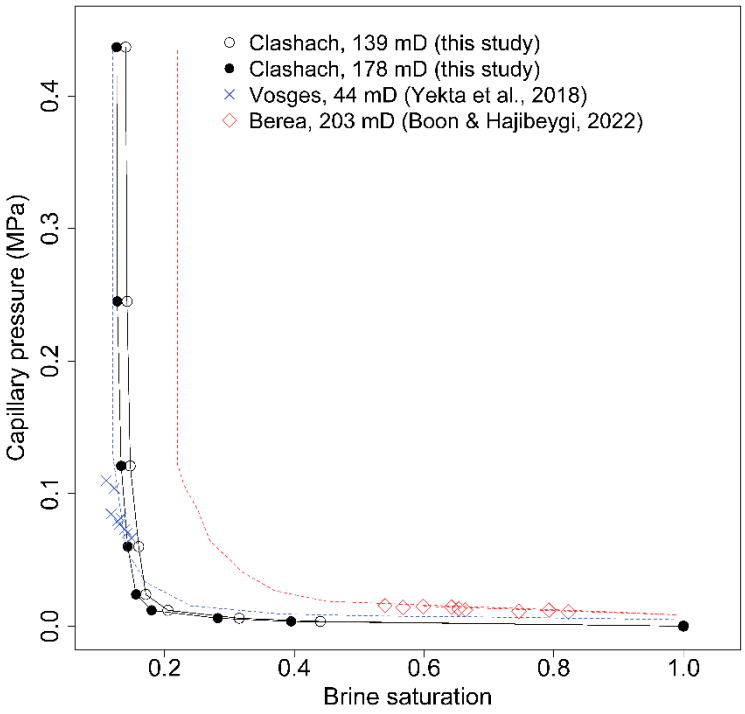

Figure 4. Hydrogen drainage capillary pressure curve for the two Clashach sandstone core plugs of our study as compared to studies by Yekta et al. [32] and Boon & Hajibeygi [47] on Vosges and Berea sandstones, respectively.

Hydrogen/brine/Clashach sandstone contact angles after imbibition were 58° at all pore fluid pressures (Fig. 2b), indicating a water-wet rock and, despite the significant cluster build-up at 7 MPa (Fig. 1e, 2b), wettability does not change with pore fluid pressure. These combined findings are in line with H_2 cluster size distributions for the same experimental data [11], which

315 show an increase in the number of intermediate size clusters at 7 MPa, without shifting the
316 cluster distribution horizontally, suggesting no wettability change.

317 The amount of H_2 residual trapping is a function of 1) the contact angle, 2) the rock porosity
318 and rock pore morphology, 3) the initial H_2 saturation and connectivity, and 4) the H_2–brine
319 IFT. The IFT of H_2–brine decreases by 1% with pressure increases from 2 to 7 MPa (from
320 73.982 to 73.293 mN m^{-1}) [33] and is hence unlikely to impact residual trapping significantly.
321 Hence, with no changes in the IFT and in the contact angle (Fig. 2b), and no change in the rock
322 porosity and rock pore morphology due to the deployment of the same Clashach sandstone
323 sample in all experiments, increased trapping at 7 MPa can only be attributed to the decreased
324 H_2 connectivity during drainage. Noteworthily, a poorer initial connectivity of hydrogen was
325 not confirmed by the repetition of primary drainage at 7 MPa (Fig. 1f) and generally, a well-
326 connected percolating cluster is expected for homogenous rock samples during drainage. It is
327 possible, that some salt precipitated during the experiments and blocked a pore throat which
328 could have altered the H_2 flow path, thereby leading to decreased initial connectivity and/or
329 increased H_2 trapping during imbibition. Salt precipitation is more pronounced at higher
330 pressures as higher pressures lead to increased drying of the brine by the injected gas [12]. The
331 increased H_2 S_{nwr} at 7 MPa is subject to further investigations. Future work should target
332 conducting repeated cyclic H_2 and brine injection experiments at 7 MPa pore fluid pressure
333 and higher, as well as experiments with H_2-saturated brine, to elucidate the reproducibility and
334 any potential effect of gas dissolution on our results. Increased trapping at higher pore fluid
335 pressure would imply that shallower (i.e. lower pressure) reservoirs are more suitable for H_2
336 storage operations. Considering the density increase of H_2 with pressure [11], a potential
337 increase in trapping with pressure implies an increase in the mass of non-recoverable H_2 per
338 volume of pore space by four orders of magnitude (from 0.16 to 1196 mg cm^{-3}).
339

340 *4.2 N_2-brine-Clashach sandstone contact angles*

341 Considering standard deviations of ~20° in our experiments, the N_2 contact angles for S_{nwi}
342 drainage and imbibition were not significantly different. Further, N_2 contact angles were not
343 significantly different from H_2 contact angles (Figs. 2 and 3). In view of similar for H_2 and N_2
344 (Fig. 1c,d, g), the similar $\theta_{receding}$ were expected. However, the N_2 S_{nwr} was >20% greater than
345 for H_2 (Fig. 1c,d, g), so a lower gas wettability, i.e. lower N_2 $\theta_{advancing}$, was anticipated. Because
346 N_2 and H_2 experiments used the same rock sample, at similar contact angle only differences in
347 the IFT could have caused the higher S_{nwr} for N_2. For any given pressure, the IFT of N_2 is lower
348 than for H_2 (SI Table S2), hence, according to theory, at similar $\theta_{advancing}$, N_2 residual
349 trapping should decrease relatively to H_2 residual trapping. The higher S_{nwr} of N_2 over H_2 is
350 subject to further investigations.

351 Higher capillary trapping of N_2 over H_2 has been shown previously in connection to an almost
352 doubled S_{nwi} of N_2 over H_2 (μCT method, Bentheimer sandstone, 1 MPa pressure and ambient
353 temperature) [31]. Here, the lower S_{nwi} of H_2 over N_2 was suspected not to be caused by
354 differences in $\theta_{receding}$ but to arise from H_2 dissolution as well as channeling, driven by the lower
355 viscosity of H_2 compared to N_2 [31]. Our data do not confirm the observations of H_2 channeling
356 during drainage (Fig. 1, [11]). Residual H_2 was distributed mainly over one side of the rock
357 sample (Fig. 1a, b, c) which could indicate some preferentiality in the H_2 fluid flow during
358 imbibition.

359

360 *4.3 Relation to other work*

361 *4.3.1 Hydrogen*

362 To date, ten studies either measured or derived H_2/brine/sandstone or pure quartz contact
363 angles. While there is general consensus in the literature that unaged H_2/brine/quartz or
364 sandstone systems are water-wet, reported contact angles seem to vary with rock type, sample

preparation and measurement methodology as well as experimental condition. Because the in-situ contact angle method captures the effects of local pore geometry and surface roughness it provides a more accurate representation of the fluid interaction in porous media than contact angle data from the tilted plate method or the captive bubble method [27]. Four studies, all conducted on Bentheimer sandstone, applied the same in-situ contact angle measurement methodology as in this work: Higgs et al. measured $\theta_{advancing}$ of 59.8° and 57° in a Soxhlet cleaned rock at ambient temperature and 0.4 MPa and 2.1 MPa, respectively [27, 33]. Jangda et al. [16] reported $\theta_{advancing}$ in a methanol-cleaned sample between 52.7° - 53.7° at 10 MPa and 323 K. Zhang et al. [31] reported $\theta_{advancing}$ of ~ 57° at ambient temperature and 1 MPa in untreated Bentheimer. All results are very close to our $\theta_{advancing}$ of 58° at 2-7 MPa and ambient temperature in a Clashach outcrop sample without further cleaning. The Bentheimer sandstone is more porous than Clashach (23% porosity vs. 12.5-13.6% porosity, respectively [11, 16, 33] and has ~ 4 % less quartz than Clashach, with correspondingly increased clay and feldspar fractions [48].

Previous reports of $\theta_{receding}$ in Bentheimer sandstone range from 44° to ~75° (1- 2.1 MPa, ambient temperature) [31, 33], a range that brackets the here measured 61°.

The captive bubble method, applied to Bentheimer and Berea sandstones, yielded significantly lower H_2/brine contact angles (25°-45°)[27, 28, 30] than the in-situ method but coincided with this study in that there was no correlation between contact angle and pressure (measured over a range of 6.9-20.7 MPa) [27, 28]. The captive bubble method was also recently used to measure H_2/brine/carbonate rock contact angles, again with no effect of increasing pressure and temperature on the contact angle [49]. However, when applied to quartz samples aged in organic acids, increasing contact angles with increasing pressure and temperature were reported [50].

389 The in-situ contact angles were also significantly higher than advancing contact angles of
390 40.8° obtained using the tilted-plate method on pure quartz (temp: 323 K, pressure:
391 25 MPa) [35]. Contrary to our study, using this method, increases in contact angles with
392 pressure and temperature from 0° to a maximum of ~50° were reported on pure, clean quartz
393 (experimental condition 1: 296 K and 0.1 MPa, condition 2: 343 K and 25 MPa) [29]. The
394 authors argued that the reported trend in contact angles was caused by the increasing
395 intermolecular quartz–gas interactions with increasing molecular gas density at increased
396 pressure [29]. While this increase in intermolecular interactions would be expected to occur for
397 any mineral, applying the tilted-plate applied to cleaned, pure mica showed no temperature and
398 pressure dependence of the contact angles with a contact angle of zero for all experimental
399 conditions (5-20 MPa, temperature 300-323K, salinity 0-213.000 ppm)[51]. In an approach to
400 explain the contact angle discrepancy in the literature, it was recently postulated that the key
401 determinant for the outcome of any fluid flow study is the type of forces acting under a given
402 experimental condition [34]: When gravitational and capillary forces dominate, as in the case
403 of the tilted plate method, there should be a clear temperature and pressure dependency on the
404 fluid injectivity and recovery, and different gases are expected to show different contact angles
405 and displacement patterns. On the other hand, when buoyancy and capillary forces dominate,
406 as for the captive bubble method, one would expect no temperature and pressure dependency
407 on the contact angle and different gases should have similar wettability and show similar
408 displacement patterns at any set experimental condition [34]. Studies by Hashemi et al. [28],
409 Higgs et al. [27] and Aghaei et al. [52] confirm this theory while the study by Esfandyari et al.
410 [50] and Abdel-Azeim et al. [51] do not. On the other hand, Abdel-Azeim et al. [51] suggested
411 that contact angles higher than zero as reported by e.g. [27-29] and apparent contact angle
412 increases with pressure [29] may stem from contamination of organic matter on the rock
413 surfaces. While this may be true for the sample in Hashemi et al. [28], Iglauer et al. [29] and

Higgs et al, [27] cleaned their rock samples using exposure to air plasma and Soxhlet extraction, respectively. A (further) source of error in contact angle measurements in artificial systems is the contamination of equipment (e.g. pumps, flow lines, cells) [27].

In real rock systems, as discussed in section 4.1, the pore morphology and porosity, the IFT and the wettability play a governing role in shaping the fluid flow, suggesting that an analysis of the results solely in terms of a dominance of buoyancy and gravitational forces may be little conclusive. Notably, cleaning of the rock sample does not seem to affect the contact angles significantly for the in-situ method (see discussion above) and the very similar contact angles in Clashach and Bentheimer sandstones suggests a negligible influence of minor variations in mineralogy and porosity. Clearly, this analysis shows that the contact angle discrepancy in the literature is not trivial, and that a structured approach is required to elucidate potential influences of methodology, experimental condition (pressure, temperature, cleaning of equipment) and -were applicable- sample preparation on the results.

The P_{cH2} curve for Clashach showed a relatively low irreducible water saturation of 12.6-14.0% in Clashach at H_2 P_c of 0.43 MPa implying a high H_2 relative permeability and H_2 storage capacity. The P_{cH2} curve for Clashach was similar to the Vosges sandstone P_c curve from [32], (derived using the results from both of the tested pressure and temperature conditions; Fig. 4), despite the significantly lower relative permeability of the Vosges sandstone. The P_c for Berea sandstone from [47] showed a higher irreducible water saturation than for Clashach and Vosges sandstone (Fig. 4). The saturations for the P_c measurements in [32], and [47] cover a small range, resulting in a higher uncertainty in the fit of the mercury injection capillary pressure data.

4.3.2 Nitrogen

Studies on N_2/brine/rock contact angles are scarce. Reported effective N_2 contact angles range from 30° on quartz (captive bubble method, 5 MPa and 313 K) [53] to 25-47° in illite and kaolinite (tilted plate method, 5-10 MPa and 60°C) [54, 55], with 3-6° higher $\theta_{receding}$ than $\theta_{advancing}$ [55], and are larger than H_2 contact angles of ~10-20° on the same minerals [54]. A stronger gas-wetting behavior of N_2 relative to H_2 [54] was indicated by our experiments but not statistically significant. Higher wettability of N_2 over H_2 would be favorable for gas separation during production if N_2 is used as a cushion gas.

Our results are close to mean in-situ N_2 contact angles of ~71° at 1 MPa and 298 K in Bentheimer sandstone [31] and to ~69° on smooth silicon in water at 5 MPa and 296 K [56]. The observed differences between $\theta_{advancing}$ and $\theta_{receding}$ correspond well with previous reports from air-water systems [57]. Our results are significantly higher than 40-60 manually measured in-situ N_2 $\theta_{receding}$ and $\theta_{advancing}$ of 34°±6° and 46°±6°, respectively, in Berea sandstone at 5.5 MPa and ambient temperature [24]. Considering 2800 times more contact angles measured in this study as well as the use of an automated approach to remove potential selection bias that might exist in manual methods, one may suspect that our study resulted in more representative answer.

5. CONCLUSION

In this work, in-situ contact angles for the H_2/brine/Clashach sandstone system were quantified at 2-7 MPa pore fluid pressure to identify any control of wettability on S_{nwr}. Measurements of N_2/brine/Clashach sandstone contact angles at 5 MPa and N_2 P_c with varying brine saturations, enabled the novel calculation of the P_{cH2} curve.

Contrary to our hypothesis, the average receding contact angles did not decrease with increasing pore fluid pressure but showed a mean of 58° at all pressures, suggesting that observed higher S_{nwr} at 7 MPa were not caused by wettability changes. Instead, the elevated

464 S_{nwr} at increased pressure was likely instigated by a decreased connectivity after drainage,
465 however decreased connectivity was not confirmed by a repetition experiment. More
466 experiments at 7 MPa and higher pressure will need to be undertaken to confirm the trend in
467 S_{nwr} with pressure. Comparison with other studies showed good alignment with other *in-situ*
468 H_2 contact angle measurements in sandstone but revealed that measurements in artificial
469 systems significantly underestimate the H_2/brine/sandstone contact angle. Overall, this study
470 and other emerging research suggests that for contact angles around 58°-70°, wettability may
471 not always be the main control for the H_2 saturation in the pore space but that H_2 dissolution
472 and channeling events may significantly affect those parameters. Overall, our results provide a
473 strong evidence base for no wettability change with pressure and help elucidating the
474 interaction between wettability and residual trapping, both of which influence H_2 storage
475 designs and predictions.

476 The P_{cH2} plays a noteworthy role in understanding how H_2 interacts within porous media.
477 When H_2 encounters a rock's pore spaces, this parameter helps quantify the onset of its
478 movement and displacement of the resident fluid, like brine. The here determined novel P_{cH2}
479 curve for Clashach sandstone showed an irreducible water saturation of 12.6-14.0% at 0.43
480 MPa, implying a high H_2 relative permeability and H_2 storage capacity.

481

482 ASSOCIATED CONTENT

483 Supporting information: TEXT S1 ´Measurements required for the calculation of the Hydrogen
484 capillary pressure´ and SI Table S2 which comprises the base results used to create Figure 4.

485

486

487 AUTHOR INFORMATION

488 **Corresponding Author**

Eike Marie Thaysen. Email: eike.thaysen@idaea.csic.es

Author Contributions

The experimental kit was built by Butler and Thaysen. Hydrogen and brine displacement experiments were carried out by Thaysen and Butler. Image reconstruction and tomographic analysis was carried out by Thaysen, Jangda, Menke and Singh. The calculation of the hydrogen capillary pressure with varying brine saturations was by Hassanpouryouzband. Interpretation of the results was by Thaysen, Butler, Heinemann and Hassanpouryouzband. The manuscript was written by Thaysen, with contributions and review from Hassanpouryouzband, Butler, Edlmann, Heinemann, Jangda, Menke and Singh. All authors have given approval to the final version of the manuscript.

Declaration of interest

The authors declare no competing interest.

ACKNOWLEDGEMENT

Thaysen, Butler, Heinemann, Hassanpouryouzband and Edlmann gratefully acknowledge the funding support from the Engineering and Physical Science Research Council (EPSRC) HyStorPor project [grant number EP/S027815/1] and from the Fuel Cells and Hydrogen 2 Joint Undertaking (JU) under grant agreement No 101006632. The JU receives support from the European Union's Horizon 2020 research and innovation programme and Hydrogen Europe and Hydrogen Europe Research.

ABBREVIATIONS

513 H_2= hydrogen, N_2= nitrogen, N_c= capillary number, P_c= capillary pressure, P_{cH2} = hydrogen
514 capillary pressure, S_{nwi} = initial saturation, S_{nwr}= residual saturation, $\theta_{advancing}$= imbibition
515 contact angle, $\theta_{receding}$= drainage contact angle, *kr*= relative permeability.
516
517
518 **References**

519 1. IPCC, *IPCC report Global Warming of 1.5 C: Summary for Policymakers.* 2018
520 2. Organization, W.H., *Fact sheets on climate change and health and biodiversity and*
521 *health* 2022.
522 3. Thaysen, E.M., et al., *Effect of dissolved H_2SO_4 on the interaction between CO_2-rich*
523 *brine solutions and limestone, sandstone and marl.* Chem Geol, 2017. **450**: p. 31-43.
524 4. Thaysen, E.M., et al., *Effects of lime and concrete waste on vadose zone carbon*
525 *cycling.* Vadose Zone J, 2014. **13**(11): p. 1-11.
526 5. Snæbjörnsdóttir, S.O., et al., *Carbon dioxide storage through mineral carbonation.*
527 Nat Rev Earth Environ, 2020. **1**: p. 90-102.
528 6. Beckingham, L.E. and L. Winningham, *Critical knowledge gaps for understanding*
529 *water-rock-working phase interactions for compressed energy storage in porous*
530 *formations.* ACS Sustain Chem Eng, 2020. **8**(1): p. 2-11.
531 7. Heinemann, N., et al., *Hydrogen storage in porous geological formations - onshore*
532 *play opportunities in the Midland Valley (Scotland, UK).* Int J Hydrog Energy, 2018.
533 **43**(45): p. 20861-20874.
534 8. Kharel, S. and B. Shabani, *Hydrogen as a long-term large-scale energy storage*
535 *solution to support renewables.* Energies, 2018. **11**(10): p. 1-17.
536 9. Heinemann, N., et al., *Enabling large-scale hydrogen storage in porous media: the*
537 *scientific challenges.* Energy Environ Sci, 2021. **14**: p. 853-864.

10. Matos, C.R., J.F. Carneiro, and P.P. Silva, *Overview of large-scale underground energy storage technologies for integration of renewable energies and criteria for reservoir identification.* J. Energy Storage, 2019. **21**: p. 241-258.
11. Thaysen, E.M., et al., *Pore-scale imaging of hydrogen displacement and trapping in porous media.* Int J Hydrog Energy, 2023. **48**(8): p. 3091-3106.
12. Hassanpouryouzband, A., et al., *Geological Hydrogen Storage: Geochemical Reactivity of Hydrogen with Sandstone Reservoirs.* ACS Energy Lett, 2022. **7**: p. 2203-2210.
13. Aftab, A., Hassanpouryouzband, A., Martin, A., Kendrick, J. E., Thaysen, E.M., Heinemann, N., Utley, J., Wilkinson, M., Haszeldine, R. S., Edlmann, K., *Geochemical Integrity of Wellbore Cements during Geological Hydrogen Storage.* Environ Sci Technol Lett, 2023. **in press**.
14. Thaysen, E.M., et al., *Estimating microbial growth and hydrogen consumption in hydrogen storage in porous media.* Renew Sustain Energ Rev, 2021. **151**(111481): p. 1-15.
15. Heinemann, N., et al., *Hydrogen storage in saline aquifers: The role of cushion gas for injection and production.* Int J Hydrog Energy, 2021. **46**: p. 39284-39296.
16. Jangda, Z., et al., *Pore-Scale Visualization of Hydrogen Storage in a Sandstone at Subsurface Pressure and Temperature Conditions: Trapping, Dissolution and Wettability.* J Colloid Interf Sci, 2022. **629**(Part B): p. 316-325.
17. Rezaei, A., et al., *Relative permeability of hydrogen and aqueous brines in sandstones and carbonates at reservoir conditions.* Geophys Res Lett, 2022.
18. Thaysen, E.M., Armitage, T., Slabon, L., Hassanpouryouzband, A., Edlmann, K., *Microbial risk assessment for underground hydrogen storage in porous rocks* Fuel, 2023. **in press**.

19. Yekta, A.E., M. Pichavant, and P. Audigane, *Evaluation of geochemical reactivity of hydrogen in sandstone: Application to geological storage.* J Appl Geochem, 2018. **95**: p. 182-194.
20. Heinemann, N., Wilinson, M., Adie, K., Edlmann,K., Thaysen, E.M.,Hassanpouryouzvband, A., Haszeldine, R.S., *Cushion Gas in Hydrogen Storage—A Costly CAPEX or a Valuable Resource for Energy Crises?* Hydrogen, 2022. **3**(4): p. 550-563.
21. Blunt, M.J., *Multiphase flow in permeable media. A Pore-scale perspective*. 2017, Cambridge, United Kingdom: Cambridge University Press.
22. Lysyy, M., G. Ersland, and M. Fernø, *Pore-scale dynamics for underground porous media hydrogen storage.* Adv Water Resour, 2022. **163**(104167): p. 1-13.
23. Morrow, N.R., *Wettability and its effect on oil recovery.* J Pet Technol, 1990. **42**(12): p. 1476–1484.
24. Khishvand, M., A.H. Alizadeh, and M. Piri, *In-situ characterization of wettability and pore-scale displacements during two- and three-phase flow in natural porous media.* Adv Water Resour, 2016. **97**: p. 270-298.
25. Scanziani, A., et al., *Automatic method for estimation of in situ effective contact angle from X-ray micro tomography images of two-phase flow in porous media.* Journal of Colloid and Interface Science, 2017. **496**: p. 52-59.
26. Muhammed, N.S., B. Haq, and D.A. Al Shehri, *Hydrogen storage in depleted gas reservoirs using nitrogen cushion gas: A contact angle and surface tension study.* International Journal of Hydrogen Energy, 2023.
27. Higgs, S., et al., *In-situ hydrogen wettability characterisation for underground hydrogen storage.* International Journal of Hydrogen Energy, 2022. **47**(26): p. 13062-13075.

28. Hashemi, L., et al., *Contact angle measurement for hydrogen/brine/sandstone system using captive-bubble method relevant for underground hydrogen storage.* Adv Water Resour, 2021. **154**(103964): p. 1-13.

29. Iglauer, S., A. Muhammad, and A. Keshavarz, *Hydrogen wettability of sandstone reservoirs: implications for hydrogen geo-storage.* Geophys Res Lett, 2020. **48**(3): p. 1-5.

30. Mirchi, V., M. Dejam, and V. Alvarado, *Interfacial tension and contact angle measurements for hydrogen-methane mixtures/brine/oil-wet rocks at reservoir conditions.* International Journal of Hydrogen Energy, 2022. **47**(82): p. 34963-34975.

31. Zhang, Y., Bijeljic, B., Gao, Y., Goodarzi, S., Foroughi, S., Blunt, M.J., *Pore-Scale Observations of Hydrogen Trapping and Migration in Porous Rock: Demonstrating the Effect of Ostwald Ripening.* Geophys Res Lett, 2023. **50**(e2022GL102383).

32. Yekta, A.E., et al., *Determination of Hydrogen-Water Relative Permeability and Capillary Pressure in Sandstone: Application to Underground Hydrogen Injection in Sedimentary Formations.* Transport in Porous Media, 2018. **122**(2): p. 333-356.

33. Higgs, S., et al., *Direct measurement of hydrogen relative permeability hysteresis for underground hydrogen storage.* International Journal of Hydrogen Energy, 2024. **50**: p. 524-541.

34. Boon, M., *Wettability of hydrogen relevant to underground hydrogen storage*, H.S.S. 2022, Editor. 2022: TU Delft. p. https://www.youtube.com/watch?v=jLmw3iBBdiY.

35. Ali, M., Jha, N.K., Al-Yaseri, A., Zhang, Y., Iglauer, S., Sarmadivaleh, M., *Hydrogen wettability of quartz substrates exposed to organic acids; Implications for hydrogen geo-storage in sandstone reservoirs.* Journal of Petroleum Science and Engineering, 2021. **207**(109081).

36. Lysyy, M., et al., *Hydrogen relative permeability hysteresis in underground storage.* Geophys Res Lett, 2022. **49**: p. 1-8.
37. Al-Yaseri, A., et al., *Initial and residual trapping of hydrogen and nitrogen in Fontainebleau sandstone using nuclear magnetic resonance core flooding.* Int J Hydrog Energy, 2022. **47**(53): p. 22482-22494.
38. Iglauer, S., et al., *Comparison of residual oil cluster size distribution, morphology and saturation in oil-wet and water-wet sandstone.* Journal of Colloid and Interface Science, 2012. **375**: p. 187-192.
39. Iglauer, S., A. Paluszny, and M.J. Blunt, *Simultaneous oil recovery and residual gas storage: A pore-level analysis using in situ X-ray micro-tomography.* Fuel, 2013. **103**: p. 905-914.
40. Pentland, C.H., et al., *Capillary trapping in water-wet sandstones: coreflooding experiments and pore-network modeling*, in *SPE International* 2010, Society of Petroleum Engineers Florence, Italy
41. AlRatrout, A., Raeini, A. Q., Bijeljic, B. & Blunt, M. J., *Automatic measurement of contact angle in pore-space images.* Advances in Water Resources, 2017. **109**: p. 158–169.
42. Hassler, G.L., Brunner. E., *Measurement of capillary pressures in small core samples.* Transactions of the AIME, 1945. **160**(01): p. 114-123.
43. Hassanpouryouzband, A., et al., *Offshore Geological Storage of Hydrogen: Is This Our Best Option to Achieve Net-Zero?* ACS Energy Lett, 2021. **6**(6): p. 2181–2186.
44. Danesh, A., *PVT and Phase Behaviour Of Petroleum Reservoir Fluids*. Vol. 47. 1998, Department of Petroleum Engineering, Heriot Watt University, Edinburgh, Scotland: Elsevier.

45. Kalantari Meybodi, M., A. Daryasafar, and M. Karimi, *Determination of hydrocarbon-water interfacial tension using a new empirical correlation.* Fluid Phase Equilibria, 2016. **415**: p. 42-50.
46. Singh, K., et al., *Time-resolved synchrotron X-ray micro-tomography datasets of drainage and imbibition in carbonate rocks.* Scientific Data, 2018. **5**(1): p. 180265.
47. Boon, M. and H. Hajibeygi, *Experimental characterization of H_2/water multiphase flow in heterogeneous sandstone rock at the core scale relevant for underground hydrogen storage (UHS).* Nat Sci Rep, 2022. **12**(14604): p. 1-11.
48. Peksa, A.E., Wolf, K. H. A. A., Zitha, P. L. J., *Bentheimer sandstone revisited for experimental purposes.* Marine and Petroleum Geology, 2015. **67**: p. 701-719.
49. Aghaei, H., Ahmed Al-Yaseri, A., Toorajipour, A., Shahsavani, B., Yekeen, N., Edlmann, K., *Host-rock and caprock wettability during hydrogen drainage:Implications of hydrogen subsurface storage.* Fuel, 2023. **351**(129048).
50. Esfandyari, H., et al., *Experimental evaluation of rock mineralogy on hydrogen-wettability: Implications for hydrogen geo-storage.* J Energy Storage, 2022. **52**(104866): p. 1-8.
51. Abdel-Azeim, S., et al., *Wettability of Caprock–H2–Water: Insights from Molecular Dynamic Simulations and Sessile-Drop Experiment.* Energy & Fuels, 2023. **37**(23): p. 19348-19356.
52. Aghaei, H., Ahmed Al-Yaseri, A., Toorajipour, A., Shahsavani, B., Yekeen, N., Edlmann, K., *Host-rock and caprock wettability during hydrogen drainage: Implications of hydrogen subsurface storage.* Fuel, 2023. **351**(129048).
53. Mills, J., M. Riazi, and M. Sohrabi. *Wettability of common rock-forming minerlas in a CO2-brine system at reservoir conditions*. in *International Symposium of the Society of Core Analysts*. 2011.

54. Al-Yaseri, A., et al., *Hydrogen wettability of clays: Implications for underground hydrogen storage.* Int J Hydrog Energy, 2021. **46**(69): p. 34356-34361.
55. Fauziah, C.A., et al., *Carbon Dioxide/Brine, Nitrogen/Brine, and Oil/Brine Wettability ofMontmorillonite, Illite, and Kaolinite at Elevated Pressure andTemperature.* Energy Fuels, 2019. **33**: p. 441-448.
56. Song, J.-W. and L.-W. Fan, *Understanding the effects of pressure on the contact angle of water on a silicon surface in nitrogen gas environment: Contrasts between low- and high-temperature regimes.* Journal of Colloid and Interface Science, 2022. **607**: p. 1571-1579.
57. Behnoudfar, D., et al., *Contact angle hysteresis: A new paradigm?* Advances in Water Resources, 2022. **161**: p. 104138.
58. Forbes, P.L., *Simple and Accurate Methods for Converting Centrifuge Data into Drainage and Imbibition Capillary Pressure Curves.* The log Analyst, 1994. **35**(4): p. 31-53.

SUPPORTING INFORMATION

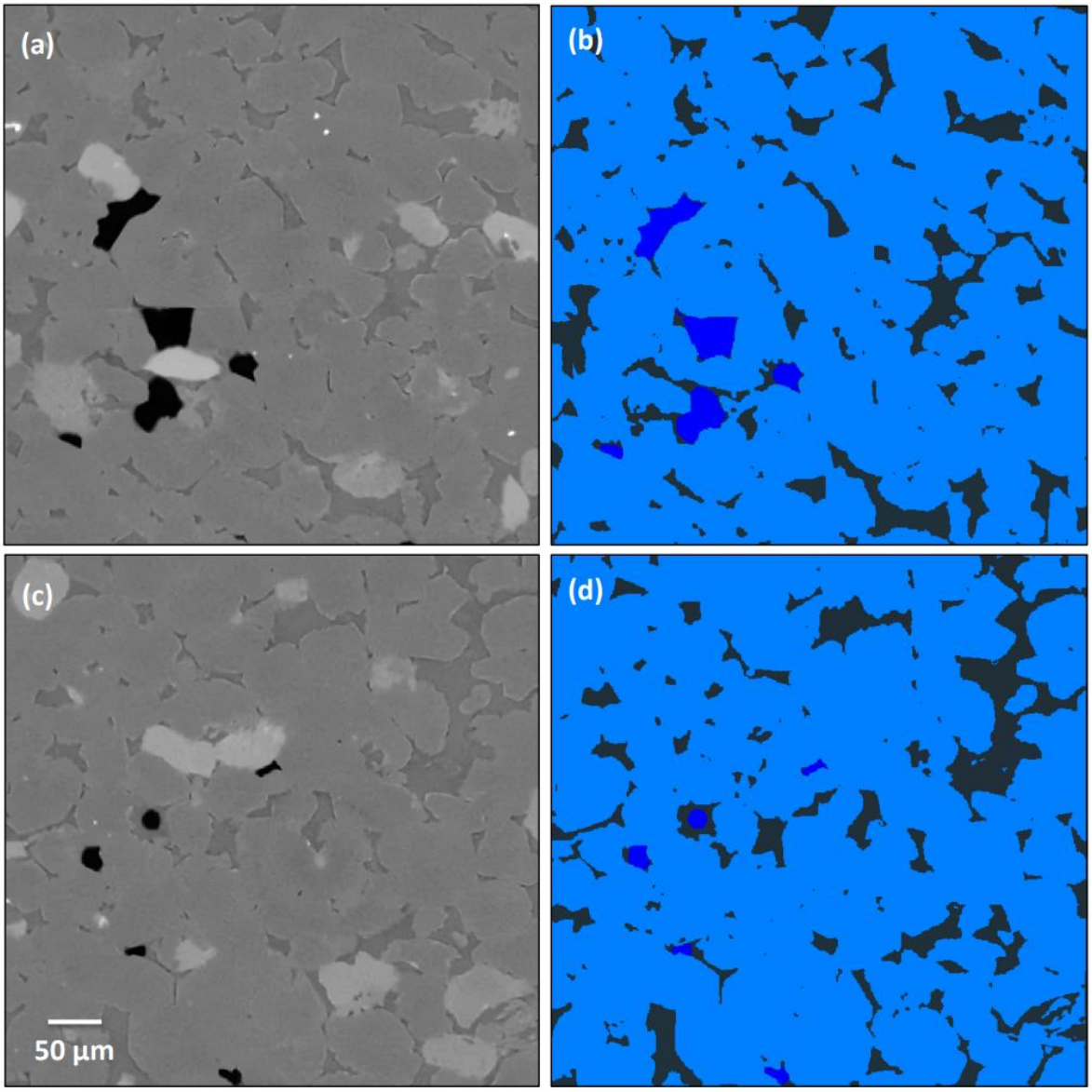

SI Fig. S1. Raw images of two distinct slices within the 500 um^3 subvolume of the Clashach sandstone core (a and c), where black colour marks hydrogen gas, light grey and white colours are grains and dark grey denotes brine. (b) and (c) show respective segmentations of the raw images in (a) and (c) where dark blue is hydrogen, light blue is grain material and black is the pore space.

TEXT S1 Measurements required for the calculation of the Hydrogen capillary pressure

Permeability to nitrogen

Two fully dried Clashach sandstone plugs (length: 5.0 cm, diameter: 3.8 cm) were each placed in a Hassler core holder (Standard Core Holder- HCH Series, Core Laboratories, UK), maintaining a sleeve pressure of 2.76 MPa. Dry nitrogen was channeled through the core plug at a consistent flow rate until the pressure readings were stable, and both the upstream and downstream pressures were documented. The steady-state permeability to nitrogen at a low mean pore pressure was determined using equation 1:

$$k_{air} = \frac{1000 \times Pa \times \mu_N \times q_N \times L}{(P_i - P_0)(P_i + P_0)/2 \times A} \quad (1)$$

where k_{air} is the permeability (mD), q_N is the flow rate of nitrogen at atmospheric pressure (cm^3/s), μ_N is the viscosity of nitrogen (cP), L is the length of core plug (cm), A is the cross-sectional area of core plug (cm^2), and Pi, Po and Pa are the upstream pressure, the downstream pressure and the atmospheric pressure, respectively (all in atm).

Helium Porosity and Grain Density

The clean and dry plug samples were first weighed. Subsequently, their grain volumes were determined using a Pycnometer System (UltraPore^{TM}300, Anton-Paar ,USA). This automated gas displacement pycnometer computes density and grain volume by assessing the pressure variation of helium within a pre-calibrated volume that expands into a matrix cup housing the plug sample. The system relies on computer-based processing for all pressure readings and calculations, effectively minimizing potential transcription errors.

Each of the clean, dry samples was placed into a designated matrix cup connected to the system. Helium, with a predetermined pressure sourced from a reference cell of known volume,

was expanded into the matrix cup, and the resultant pressure was recorded. Using Boyle's Law, grain volumes were computed based on a modified version of the standard equations:

Boyle's Law calculation $$P_1V_1 = P_2V_2 \quad (2)$$

Grain volume calculation $$P_1V_{ref} = P_2 (V_{ref} + V_{matrix} - V_g - V_{disk}) \quad (3)$$

Therefore:

$$V_g = ((V_{matrix} + V_{ref}) - (P_1/ P_2. V_{ref})) - V_{disk} \quad (4)$$

where P_1 and P_2 are the pressure of helium in the reference cell and after expansion into matrix cup, respectively, V_{ref} is the volume of the reference cell, V_{matrix} is the volume of the matrix cup, V_g is the grain volume of the plug sample, and V_{disk} is the disk volume added to cup to reduce dead space. To determine the true grain volume, the volume of any mounting material was accounted for and subtracted.

The system is equipped with a precision 0-1.37 MPa transducer. Its linearity and hysteresis have an impressive accuracy, registering less than +/- 0.11% of full scale. To ensure its precision, the system undergoes calibration twice daily using steel disks with known volumes. These disks receive their calibration externally. The calibration correlation factor must consistently fall within the range of 1.0000 +/- 0.0001 for validity. For enhanced accuracy, beyond the regular calibrations, check plugs are measured roughly after every ten samples. At the conclusion of each worksheet, at least one sample undergoes a double-check to ensure consistency.

Grain density was derived from the grain volume and the dry weight of the sample. Adjustments were made for the weight of any mounting material when necessary. Bulk volume (V_b) was ascertained using mercury displacement. Subsequently, pore volume (V_p) and porosity (ϕ) were computed according to equations 5 and 6:

$$V_p = V_b - V_g \quad (5)$$

$$\phi = V_p / V_b \quad (6)$$

Table S1 shows the results of the N_2 permeability, the porosity and the grain density measurements.

SI Table S1. Permeability and Porosity of Clashach core samples

Plug	K_{N2}, millidarcies	Porosity, frac	Grain density, g/cc
1	139	0.130	2.64
2	178	0.131	2.64

Core Sample Saturation with 0.5 M Caesium Chloride

The clean and dry Clashach sandstone plugs were first weighed. Subsequently, they were placed inside a sealed container and subjected to evacuation for a period of 24 hours. After the evacuation, the container was filled with the same brine that was utilized for the H_2 and brine core-flood experiments (0.5 M CsCl). The brine was then pressurized to 13.8 MPa, and this pressure was sustained for an additional 24 hours.

After the stipulated time, the brine pressure was gently released. The samples, now saturated with brine, were extracted from the container and weighed. The difference in weight between the dry and saturated samples serves as an indicator of the brine volume within each sample. This value was collated with the pore volume deduced from helium injection.

In addition, every brine-saturated sample was weighed when submerged in the saturating brine. Utilizing Archimedes' principle, a bulk volume was computed. Saturation porosity was then determined using the derived saturation pore volume and the calculated Archimedes bulk volume. This saturation porosity was subsequently compared to the porosity determined through helium injection.

Capillary Pressure Determination

The Clashach sandstone plugs were pressure-saturated with 0.5 M CsCl, as detailed in section 2.3.3. Each plug was positioned in a rotor bucket equipped with a graduated receiving tube and mounted onto the body of a high-speed centrifuge. The centrifuge employed was an ACES200—an automated, camera-enabled system that incorporated a modified Beckman L100 Optima centrifuge with its associated control software.

The receiving tube and the void around each sample were filled with the displacing phase, which in this context, is air. The rotor can accommodate up to three 1.5-inch diameter plugs simultaneously. In scenarios where brine saturation diminishes (like in drainage, which is the case here), the receiving tubes are strategically positioned farther from the rotation's center than the plugs, ensuring efficient brine collection.

The rotor, loaded with the plugs, was subjected to varied rotation speeds, ranging between 800 to 7500 rpm. These speeds were chosen to generate equivalent capillary pressures (*Pc*) within a spectrum of approximately 0.02 MPa to around 2.07 MPa, especially for an air-displacing-brine mechanism. While the rotor was spinning, a stroboscopic light illuminated the receiving tube to determine the volume of brine displaced from each plug. Readings can be taken either manually or captured with a camera. In this case, we recorded the readings manually. Every core plug was retained at each specific capillary pressure until it reached

equilibration for the given pressure. After a span ranging from 24 to 48 hours, equilibration was confirmed if the fluid volume displaced from each core plug remained unaltered for a consecutive 4-hour period. The rotor bucket assemblies' weights were recorded before and [42] post-test to identify any potential evaporative losses. The volumes of brine displaced, plug pore volumes, and the respective capillary pressures derived from test parameters were utilized to deduce capillary pressure and saturation data. Further details about the method can be found elsewhere [42].

Calculation of Centrifuge Air-Brine Capillary Pressure from Brine Displacement Data

Average brine saturations were adjusted for capillary end effects, and the end-face brine saturations were derived using Pierre Forbes' methodology [58]. Capillary Pressure (P_c) was deduced from the rotation rates via equation 7:

$$P_c = 1.578\text{x}10^{-7} \times (\rho_b - \rho_{air}) \times (R - L/2) \times L \times RPM^2 \quad (7)$$

where ρ_b is density of brine (1.06 g/cm^3), ρ_{air} is the density of air (0.0012 g/cm^3), R is the distance from centre of rotation to outer face of the core plug in cm, L is the length of core plug in cm, and RPM are revolutions per minute. From the above relationship it can be seen that the capillary pressure generated for each sample at each spin speed can be different due any differences in plug length.

The average brine saturation, Sw_{avg}, is determined using equation 8:

$$Sw_{avg} = \frac{Vp - V_{displaced}}{Vp} \quad (8)$$

where Vp is the pore volume in cm^3 and $V_{displaced}$ is the volume of displaced fluid in cm^3. Capillary pressure curves for each sample were derived using Forbes' equations [58]. The results, presented in both tabular and graphical formats, include inlet end-face brine saturations

798 SI Table S2. Parameters required for calculation of the H_2 capillary pressure using the N_2 capillary pressure data. P_c= capillary pressure, ψ=

799 conversion factor. Percentages after the density and IFT parameters denote the standard deviations of the mean.

N_2 P_c (MPa)	Brine Sat. Sample 1	Brine Sat. Sample 2	Density N_2 (kg/m^3) ± 0.1%	Density H_2 (kg/m^3) ± 0.1%	Density 0.5 M CsCl (kg/m^3)	IFT N_2 (mlN/m) ± 1%	IFT H_2 (mlN/m) ± 1%	Wettability N_2 (Cos(θ))	Wettability H_2 (Cos(θ))	N_2/Brine density difference	H_2/Brine density difference	Density Difference Ratio	IFT Ratio	Wettability ratio	ψ	H_2 P_c (MPa)
0	1	1	0	0	0	0	0	0	0	0	0	0		0	0	0
0.003	0.44	0.395	0.237794532	0.017106	1,057.80	75.846	75.89	0.406737	0.484809	1057.562	1057.783	0.999791	1.00058	1.19195	1.1924	0.0035772
0.005	0.315	0.282	0.3963429	0.028508	1,057.81	75.812	75.887	0.406737	0.484809	1057.414	1057.781	0.999652	1.000989	1.19195	1.1927	0.0059636
0.01	0.205	0.18	0.79274184	0.057004	1,057.83	75.725	75.882	0.406737	0.484809	1057.037	1057.773	0.999304	1.002073	1.19195	1.1936	0.0119359
0.02	0.171	0.156	1.58573586	0.113962	1,057.85	75.552	75.871	0.406737	0.484809	1056.264	1057.736	0.998609	1.004222	1.19195	1.1953	0.0239063
0.05	0.16	0.143	3.966231	0.284558	1,057.94	75.04	75.837	0.406737	0.484809	1053.974	1057.655	0.996519	1.010621	1.19195	1.20004	0.0600208
0.1	0.147	0.133	7.9383462	0.56794 8	1,058.08	74.204	75.782	0.406737	0.484809	1050.142	1057.512	0.99303	1.021266	1.19195	1.2088	0.1208813
0.2	0.142	0.127	15.8982678	1.131278	1,058.37	72.598	75.672	0.406737	0.484809	1042.472	1057.239	0.986032	1.042343	1.19195	1.2251	0.2450133
0.35	0.14	0.126	27.8656098	1.967676	1,058.80	70.347	75.511	0.406737	0.484809	1030.934	1056.832	0.975495	1.073408	1.19195	1.2481	0.4368331

800

801